nanomaterials

MDPI

Article

Shape-Factor Impact on a Mass-Based Hybrid Nanofluid Model for Homann Stagnation-Point Flow in Porous Media

Shiyuan Li [1,2,*] and Xiangcheng You [1]

[1] College of Petroleum Engineering, China University of Petroleum-Beijing, Beijing 102249, China
[2] State Key Labortory of Petroleum Resources and Prospecting, Beijing 102249, China
* Correspondence: lishiyuan1983@cup.edu.cn

Abstract: This paper studies the impact of shape factor on a mass-based hybrid nanofluid model for Homann stagnation-point flow in porous media. The HAM-based Mathematica package BVPh 2.0 is suitable for determining approximate solutions of coupled nonlinear ordinary differential equations with boundary conditions. This analysis involves discussions of the impact of the many physical parameters generated in the proposed model. The results show that skin friction coefficients of Cf_x and Cf_y increase with the mass of the first and second nanoparticles of the hybrid nanofluids w_1 and w_2 and with the coefficient of permeability in porous media. For the axisymmetric case of $\gamma = 0$, when $w_1 = w_2 = 10$ gr, $w_f = 100$ gr and $Cf_x = Cf_y = 2.03443$, 2.27994, 2.50681, and 3.10222 for $\sigma = 0$, 1, 2, and 5. Compared with $w_1 = w_2 = 10$ gr, $w_f = 100$ gr, and $\sigma = 0$, it can be found that the wall shear stress values increase by 12.06%, 23.21%, and 52.48%, respectively. As the mass of the first and second nanoparticles of the mass-based hybrid nanofluid model increases, the local Nusselt number Nu_x increases. Values of Nu_x obviously decrease and change with an increase in the coefficient of permeability in the range of $\gamma < 0$; otherwise, Nu_x is less affected in the range of $\gamma > 0$. According to the calculation results, the platelet-shaped nanoparticles in the mass-based hybrid nanofluid model can achieve maximum heat transfer rates and minimum surface friction.

Keywords: mass-based hybrid nanofluids; Homann stagnation-point flows; shape factor; porous media

check for updates

Citation: Li, S.; You, X. Shape-Factor Impact on a Mass-Based Hybrid Nanofluid Model for Homann Stagnation-Point Flow in Porous Media. *Nanomaterials* **2023**, *13*, 984. https://doi.org/10.3390/nano13060984

Academic Editors: Henrich Frielinghaus, Frederik Tielens and Sergio Brutti

Received: 10 February 2023
Revised: 25 February 2023
Accepted: 5 March 2023
Published: 8 March 2023

1. Introduction

A hybrid nanofluid consists of two kinds of nanofluids combined in a base fluid. Hybrid nanofluids have become a hot field of interest for researchers in engineering applications of various disciplines and industries, such as the heat transfer of nanofluids in micro-channel or porous media, geothermal applications, oil-flow filtration, and so on [1–8].

It is of great interest to researchers to apply hybrid nanoparticles and to determine how the shape of nanoparticles influences thermophysical properties. Murshed et al. [9] used deionized water as the medium to prepare nanofluids from spherical and rod-shaped TiO_2 nanoparticles. In addition to nanoparticle volume fraction, nanoparticle sizes and shapes also contribute to the enhancement of thermal conductivity. Alumina nanoparticles of different shapes were examined by Timofeeva et al. [10] in a mixture of ethylene glycol and water to determine their thermal conductivity and viscosity. The viscosity and thermal conductivity of nanofluids with approximate rectangular and spherical shapes were studied experimentally by Jeong et al. [11]. The significant effects of nanoparticle shapes on viscosity and thermal conductivity were observed in the volume concentration range of 0.05–5.0 vol%. In a study by Elias et al. [12], different nanoparticle shapes were examined with regard to the performance of shell-and-tube heat exchangers using five shapes of nanoparticles. As a result, the cylindrical nanoparticles demonstrated better heat transfer characteristics and an even higher rate of heat transfer. An analysis of heat transfer and fluid-flow characteristics was conducted by Vanaki et al. [13] using SiO_2 nanoparticles of different concentrations and shapes. In terms of heat transfer enhancement, SiO_2-EG

nanofluids with platelet-shaped nanoparticles exhibited the highest performance. Using a stretch sheet, Ghadikolaei et al. [14] studied the effects of induced magnetic fields on stagnant flows of hybrid nanofluids. The effect of temperature distribution on the shape of hybrid nanofluids was studied. Generally, platelet-shaped nanoparticles proved to be more effective than brick-shaped, cylindrical, and spherical nanoparticles. The effects of magnetic force and radiation on alumina migration in permeable media were simulated by Sheikholeslami et al. [15] using a new numerical method. In order to enhance the characteristics of the working liquid, Al_2O_3-water with various nanoparticle shapes was selected. In an isothermal heated horizontal tube, Benkhedda et al. [16] conducted numerical simulations of the steady-state forced-convection heat transfer and fluid-flow characteristics of hybrid nanofluids of various shapes. Nanoparticles with bladed shapes exhibited the highest heat transfer rate when the volume concentration was high, followed by those with platelet, cylindrical, or spherical shapes. Depending on the different shapes and radiation levels of the nanoparticles, the hydrothermal properties of Al_2O_3-H_2O nanofluids passing through a porous shell under ambient magnetic conditions were studied by Shah et al. [17] and Khashi'ie et al. [18]. You et al. [19–21] studied the flow characteristics of Cu-Al_2O_3-H_2O hybrid nanofluids in the inclined microchannel of porous media. A smaller average spherical particle size and a high concentration of small particles enhanced the heat transfer within the nanofluid. Wanatasanappan et al. [22] carried out experimental research on the viscosity and rheological properties of hybrid nanofluids, analyzed the influence of Al_2O_3-Fe_2O_3 mixing ratios on viscosity properties, and established a correlation with viscosity prediction. Using a rotating disk with a constant radial stretching rate, Dinavand et al. [23] explored the three-dimensional laminar flow of a hybrid nanofluid in an incompressible, steady condition. Calculations for the hybrid single-phase nanofluid model were based on the mass of nanoparticles in conjunction with the mass of the base fluid at a constant pressure. For the flow of an incompressible, two-dimensional, hybrid nanofluid on a convection-heated moving wedge with a radiation transition, Berrehal et al. [24] calculated the steady flow using numerical simulation. Spherical and non-spherical nanoparticle suspensions of magnetite (Fe_3O_4) and graphene oxide (GO) were suspended in pure water. Rahimi et al. [25] studied two-dimensional natural convection and entropy generation in a hollow heat exchanger filled with a CuO-water nanofluid. The KKL model was used to estimate the dynamic viscosity of nanoparticles based on their shape in the simulation. In nanofluid-filled channels, Rao et al. [26] considered fluid flow, heat transfer, entropy generation, and hot-wire visualization using the finite volume method. A Koo–Kleinstreuer–Li model was used to estimate dynamic viscosity, and Brownian motion was taken into account. In horizontal microchannels, Soumya et al. [27] examined the flow and thermal properties of Fe_3O_4-Ag/water and Fe_3O_4-Ag/kerosene hybrid nanofluids and analyzed the effect of different nanoparticle shape factors on nanofluid temperature. The perturbation technique was used by Subray et al. [28] to study the effect of the nanoparticle shape factor on convective heat and mass transfer in an inclined pipe. The thermal conductivity of SWCNT-CuO (25:75)/water nanofluids was investigated by Esfe et al. [29] using basic parameters such as temperature and the solid volume fraction. A permeable exponentially shrinking Riga surface with thermal radiation energy was considered by Mandal et al. [30] to determine the flow of hybrid Ag-MoS_2/water nanofluids. They investigated the velocity, temperature, surface friction coefficients, the Nusselt number, and entropy generation at the contraction Riga surface under convective heat boundary conditions, as well as the way hybrid nanofluids varied in viscosity, thermal conductivity, and slip velocity. Farooq et al. [31] studied the velocity, thermal field, and entropy distribution characteristics of hybrid nanofluids when passing through a thermal radiation slurry. With Cattaneo–Christov heat flux, carbon nanotubes were used as nanoparticles, and ethylene glycol was used as a base fluid. Utilizing X-ray-computed tomography and 3D scanning transmission electron microscopy, Li et al. [32] characterized the combined effects of nanofiller volume fractions and packer–polymer interface interactions. As a means of improving heat transfer capacity, Qi et al. [33] developed a contact probability model for analyzing silicone rubber

composites with hybrid fillers in terms of thermal conductivity. In both experimental and simulation studies, the volume fraction, filler shape, and filler size were found to be the most significant factors that affect a composite material's thermal conductivity. Using water-based Fe_3O_4-Al_2O_3-ZnO nanofluid, Adun et al. [34–36] investigated the effect of temperature, volume concentration, and mixing ratio on the fluid. Machine learning models were also developed for predicting the fluid's characteristics. Similarly, ternary hybrid nanofluids were studied for thermal conductivity and dynamic viscosity.

There are many references on stagnation point flow, some of which are studied in the following literature survey. Ariel [37] studied the two-dimensional stagnation-point flow problem of second-order non-Newtonian fluids. Weidman [38,39] changed exterior potential flow in Homann's problem and solved non-axisymmetric stagnation-point flows and rotational stagnation-point flows. Dinarvan et al. [40] solved Tiwari–Das nanofluid models by using Homotopy Analysis Method (HAM), and observed transient MHD stagnation-point and heat transfer over a vertically permeable sheet for nanofluids. Othman et al. [41] investigated numerically steady flow of two-dimensional mixed convection boundary layers near stagnation on impermeable vertical surfaces that are stretching and shrinking. It was investigated by Abbas et al. [42] whether stagnation-point flows occurred in MHD micropolar nanomaterial fluid flowing around a sinusoidally shaped cylinder. In addition, the velocity slip of porous surfaces was also studied. Turkyilmazoglu [43] mainly used numerical and perturbation methods to study the unsteady flow field caused by the deceleration of a rotating ball. A vertically stretched thin plate was examined by Sharma et al. [44] for effects of heat generation and absorption on mixed-convection stagnation-point flows with external magnetic fields. The magneto-hydrodynamic oscillatory oblique stagnation-point flows of micropolar nanofluids were analyzed by Sadiq et al. [45]. Copper and alumina nanoparticles were studied while the aqueous base solution was observed. Ahmed et al. [46] used Tiwari and Das models to study heat transfer characteristics of hybrid nanofluids in non-axisymmetric Homann stagnation region with magnetic flux. The importance of the shape factors of nanoparticles, namely cylinders, blades, bricks and platelets, was studied under free flow conditions independent of time. Khan et al. [47] considered unsteady three-dimensional non-axisymmetric Homann flows of conducting nanofluids under buoyancy. By using the fourth-order Runge–Kutta method combined with shooting techniques, Mahapatra et al. [48] developed a numerical method to solve nonaxisymmetric Homann stagnation-point flows on a rigid plate of viscoelastic fluid. Khan et al. [49] studied Homann stagnation-point flows of non-axisymmetric Walter's B nanofluids, and cylindrical disk exhibited nonlinear Rosseland thermal radiation and magnetohydrodynamics that was independent of time. As described in Waini et al. [50], hybrid nanofluid flows on a flat plate with non-axisymmetric stagnation points are studied.

This study applies the homotopy analysis method (HAM) to approximate analytical solutions for shape-factor impact on a mass-based hybrid nanofluid model for Homann stagnation-point flow in porous media. Some HAM-based packages developed in Maple or Mathematica simplify its application. The free software BVPh 2.0 can be downloaded online (http://numericaltank.sjtu.edu.cn/BVPh.htm (accessed on 18 May 2013)). It is an easy-to-use tool that calculates boundary layer flows [51,52]. This paper is divided into four sections. In addition to the introduction in Section 1, Section 2 contains mathematical descriptions of this problem. Section 3 covers the results and discussion and includes graphic illustrations and tables. Finally, Section 4 contains the conclusions, highlighting the main findings in this work.

2. Mathematical Formulas

A mass-based hybrid nanofluid model for Homann stagnation-point flow in porous media is shown in Figure 1. The $\overline{z}$-axis represents normal direction and $\overline{xy}$ represents a plane in Cartesian coordinate systems. The governing equations are as follows (Weidman [38]; Waini et al. [50]):

$$\frac{\partial \overline{u}}{\partial \overline{x}} + \frac{\partial \overline{v}}{\partial \overline{y}} + \frac{\partial \overline{w}}{\partial \overline{z}} = 0, \tag{1}$$

$$\overline{u}\frac{\partial \overline{u}}{\partial \overline{x}} + \overline{v}\frac{\partial \overline{u}}{\partial \overline{y}} + \overline{w}\frac{\partial \overline{u}}{\partial \overline{z}} = \overline{u}_e\frac{d\overline{u}_e}{d\overline{x}} + \frac{\mu_{hnf}}{\rho_{hnf}}\frac{\partial^2 \overline{u}}{\partial \overline{z}^2} - \frac{\mu_{hnf}}{K\rho_{hnf}}(\overline{u} - \overline{u}_e), \tag{2}$$

$$\overline{u}\frac{\partial \overline{v}}{\partial \overline{x}} + \overline{v}\frac{\partial \overline{v}}{\partial \overline{y}} + \overline{w}\frac{\partial \overline{v}}{\partial \overline{z}} = \overline{v}_e\frac{d\overline{v}_e}{d\overline{x}} + \frac{\mu_{hnf}}{\rho_{hnf}}\frac{\partial^2 \overline{v}}{\partial \overline{z}^2} - \frac{\mu_{hnf}}{\overline{K}\rho_{hnf}}(\overline{v} - \overline{v}_e), \tag{3}$$

$$\overline{u}\frac{\partial \overline{T}}{\partial \overline{x}} + \overline{v}\frac{\partial \overline{T}}{\partial \overline{y}} + \overline{w}\frac{\partial \overline{T}}{\partial \overline{z}} = \frac{\overline{k}_{hnf}}{(\rho c_p)_{hnf}}\frac{\partial^2 \overline{T}}{\partial \overline{z}^2}, \tag{4}$$

subject to

$$\begin{array}{l} \overline{u} = 0,\ \overline{v} = 0,\ \overline{w} = 0,\ \overline{T} = \overline{T}_w(x) \quad at \quad \overline{z} = 0 \\ \overline{u} \to \overline{u}_e(x),\ \overline{v} \to \overline{v}_e(x),\ \overline{w} \to \overline{w}_e(x),\ \overline{T} \to \overline{T}_\infty \quad at \quad \overline{z} \to \infty \end{array}, \tag{5}$$

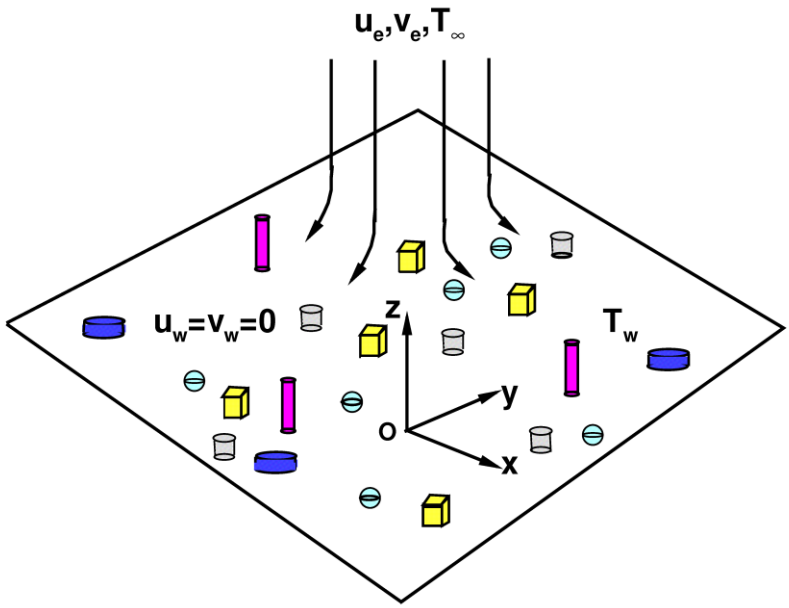

Figure 1. Physical model and coordinate systems.

In the formulas, $\overline{u}, \overline{v}, \overline{w}$ represent velocity components, external flow velocities are $\overline{u}_e(\overline{x}, \overline{y}) = \overline{x}\left(\overline{a} + \overline{b}\right)$, $\overline{v}_e(\overline{x}, \overline{y}) = \overline{y}\left(\overline{a} - \overline{b}\right)$, and $\overline{w}_e(\overline{z}) = -2\overline{a}\overline{z}$ such that $\overline{a}, \overline{b}$ represent shear–strain rates; surface temperature is represented by $\overline{T}_w = \overline{T}_\infty + \overline{T}_0\overline{x}$ ($\overline{T}_0$ represents characteristic temperature and $\overline{T}_\infty$ represents ambient temperature); $\overline{K}$ represents the permeability of porous media; $\overline{k}$ represents conductivity at certain temperatures; ρ represents fluid density; c_p represents the specific heat capacity coefficient; and μ represents dynamic viscosity. Table 1 shows the thermophysical properties of H_2O, Cu, and Al_2O_3 nanoparticles. Tables 2 and 3 present mass-based hybrid nanofluid models for the thermophysical properties of spherical nanoparticles.

Table 1. Properties of H_2O and nanoparticles [6,18,23,24].

Properties	ρ (kg/m^3)	k (W/mK)	c_p (J/kgK)
H_2O	997.1	0.613	4179
Cu	8933	401	385
Al_2O_3	3970	40	765

Table 2. Mass-based hybrid nanofluid models for thermophysical properties [23,24,53].

Properties	Formulation
Heat capacitance	$(\rho c_p)_{hnf} = \phi(\rho c_p)_s + (1-\phi)(\rho c_p)_f$
Density	$\rho_{hnf} = \phi\rho_s + (1-\phi)\rho_f$
Dynamic viscosity	$\mu_{hnf} = \frac{\mu}{(1-\phi)^{2.5}}$ (Spherical)
	$\mu_{hnf} = (1 + A\phi + B\phi^2)\mu_f$ (Non-spherical)
Thermal conductivity	$\frac{k_{hnf}}{k_{nf}} = \frac{k_{s2}+(n_2-1)k_{nf}-(n_2-1)\phi_2(k_{nf}-k_{s2})}{k_{s2}+(n_2-1)k_{nf}+\phi_2(k_{nf}-k_{s2})}$
	$\frac{k_{nf}}{k_f} = \frac{k_{s1}+(n_1-1)k_f-(n_1-1)\phi_1(k_f-k_{s1})}{k_{s1}+(n_1-1)k_f+\phi_1(k_f-k_{s1})}$

Table 3. The mass-based models for selective hybrid nanofluids [23,24,53].

Properties	Mathematical Relations
Equivalent density	$\rho_s = \frac{(\rho_1\times w_1)+(\rho_2\times w_2)}{w_1+w_2}$
Specific heat equivalent of nanoparticles at constant pressure	$(c_p)_s = \frac{((c_p)_1\times w_1)+((c_p)_2\times w_2)}{w_1+w_2}$
Solid volume fraction of first nanoparticle	$\phi_1 = \frac{\frac{w_1}{\rho_1}}{\frac{w_1}{\rho_1}+\frac{w_2}{\rho_2}+\frac{w_f}{\rho_f}}$
Solid volume fraction of second nanoparticle	$\phi_2 = \frac{\frac{w_2}{\rho_2}}{\frac{w_1}{\rho_1}+\frac{w_2}{\rho_2}+\frac{w_f}{\rho_f}}$
Equivalent volume fraction of nanoparticles	$\phi = \phi_1 + \phi_2 = \frac{\frac{w_1+w_2}{\rho_s}}{\frac{w_1+w_2}{\rho_s}+\frac{w_f}{\rho_f}}$

It is worth noting that w_1, w_2, w_f are the masses of the first and second nanoparticles and base fluid water, respectively; ϕ_1,ϕ_2 represent Cu and Al_2O_3 nanoparticles, respectively; and solid compositions are represented by the subscripts $n1$ and $n2$. $\phi = \phi_1 + \phi_2$ is the volume fraction of hybrid nanofluids, and n is the shape factor, $n = 3/\psi$, where ψ represents the sphericity of nanoparticles. Table 4 shows A and B coefficients for non-spherical nanoparticles in the effective viscosity relation for nanoparticles of different shapes.

Table 4. Sphericity, empirical shape factor, and A, B for non-spherical nanoparticles [18,23–25].

Nanoparticle Shape	Sphere	Brick	Cylinder	Platelet	Disk
n	3	3.7	4.8	5.7	8.3
ψ	1	0.81	0.62	0.52	0.36
A		1.9	13.5	37.1	14.6
B		471.4	904.4	612.6	123.3

Using similarity transformation (Weidman [38]; Waini et al. [50]), we obtain

$$\begin{aligned} &\bar{u} = \bar{x}f\prime(\eta)\left(\bar{a}+\bar{b}\right),\ \bar{v} = \bar{y}g\prime(\eta)\left(\bar{a}-\bar{b}\right),\ \bar{w} = -\sqrt{\bar{a}\nu_f}\left[f(\eta)\left(\bar{a}+\bar{b}\right)+g(\eta)\left(\bar{a}-\bar{b}\right)\right] \\ &\theta = \frac{\bar{T}-\bar{T}_\infty}{\bar{T}_w-\bar{T}_\infty},\ \eta = \bar{z}\sqrt{\frac{\bar{a}}{\nu_f}} \end{aligned}, \quad (6)$$

In the formula, ′ indicates the derivative with respect to η.
Substitute Equation (6) into Equations (1)–(4), and one gets:

$$N_f(f,g) = A_1 f''' + (1+\gamma)\left(ff''+1-f\prime^2\right) + (1-\gamma)gf'' - A_1\sigma(f\prime-1) = 0, \quad (7)$$

$$N_g(f,g) = A_1 g''' + (1-\gamma)\left(gg''+1-g\prime^2\right) + (1+\gamma)fg'' - A_1\sigma(g\prime-1) = 0, \quad (8)$$

$$N_\theta(f,g,\theta) = \frac{A_2}{\Pr}\theta'' + (1+\gamma)(f\theta\prime - f\prime\theta) + (1-\gamma)g\theta\prime = 0, \tag{9}$$

subject to

$$\begin{array}{l} f(0) = 0,\ f\prime(0) = 0,\ g(0) = 0,\ g\prime(0) = 0,\ \theta(0) = 1 \\ f\prime(\eta) \to 1,\ g\prime(\eta) \to 1,\ \theta(\eta) \to 0 \quad at \quad \eta \to \infty \end{array}, \tag{10}$$

In the formula, $N_f(f,g)$, $N_g(f,g)$, $N_\theta(f,g,\theta)$ are nonlinear differential operators; the reflective symmetries are obtained through $f(\eta,\gamma) = g(\eta,-\gamma)$ or $f(\eta,-\gamma) = g(\eta,\gamma)$, where γ is the ratio of the strain–shear rate. The coefficients of A_1, A_2, σ, and Pr are given by

$$A_1 = \frac{\mu_{hnf}/\mu_f}{\rho_{hnf}/\rho_f},\ A_2 = \frac{k_{hnf}/k_f}{(\rho c_p)_{hnf}/(\rho c_p)_f},\ \gamma = \frac{b}{a},\ \sigma = \frac{\nu_f}{aK},\ \Pr = \frac{\mu_f(c_p)_f}{k_f}. \tag{11}$$

The skin friction coefficients of Cf_x, Cf_y and the local Nusselt number Nu_x are

$$\overline{C}_{fx} = \frac{\mu_{hnf}}{\rho_f u_e^2}\left(\frac{\partial \overline{u}}{\partial \overline{z}}\right)_{\overline{z}=0},\ \overline{C}_{fy} = \frac{\mu_{hnf}}{\rho_f v_e^2}\left(\frac{\partial \overline{v}}{\partial \overline{z}}\right)_{\overline{z}=0},\ \overline{Nu}_x = -\frac{\overline{x}k_{hnf}}{k_f(\overline{T}_w - \overline{T}_\infty)}\left(\frac{\partial \overline{T}}{\partial \overline{z}}\right)_{\overline{z}=0}, \tag{12}$$

$$\begin{array}{l} C_{fx} = \sqrt{\mathrm{Re}_x(1+\gamma)}\overline{C}_{fx} = \frac{\mu_{hnf}}{\mu_f}f''(0),\ C_{fy} = \sqrt{\mathrm{Re}_y(1-\gamma)}\overline{C}_{fy} = \frac{\mu_{hnf}}{\mu_f}g''(0) \\ Nu_x = \sqrt{\frac{1+\gamma}{\mathrm{Re}_x}}\overline{Nu}_x = -\frac{k_{hnf}}{k_f}\theta''(0) \end{array}, \tag{13}$$

In the formulas, the local Reynolds numbers are $\mathrm{Re}_x = u_e x/\nu_f$, and $\mathrm{Re}_y = v_e y/\nu_f$. HAM-based Mathematica packages [48,49] are suitable for determining approximate solutions of coupled nonlinear ordinary differential Equations (7)–(9) with Boundary Conditions (10). Free online instructions for BVPh 2.0 are available online (http://numerical-tank.sjtu.edu.cn/BVPh.htm (accessed on 18 May 2013)).

As a result, HAM based on topological homotopy transforms a nonlinear problem into an infinite linear subproblem without requiring any physical parameters. The problems considered have the following characteristics:

$$f(\eta) = \sum_{m=0}^{+\infty} f_m(\eta),\ g(\eta) = \sum_{m=0}^{+\infty} g_m(\eta),\ \theta(\eta) = \sum_{t=0}^{+\infty} \theta_m(\eta), \tag{14}$$

In the formula, $f_m(\eta)$, $g_m(\eta)$, $\theta_m(\eta)$ are calculated based on the higher-order deformation equation controlled by the selected auxiliary linear operator. In accordance with Equations (7)–(9) and the Boundary Conditions (10) at infinity, $f(\eta)$, $g(\eta)$, $\theta(\eta)$ should be in the form

$$f(\eta) = \sum_{k=0}^{+\infty}\sum_{i=0}^{+\infty}\sum_{j=0}^{+\infty} a_{i,j}^k \eta^i e^{-j\eta},\ g(\eta) = \sum_{k=0}^{+\infty}\sum_{i=0}^{+\infty}\sum_{j=0}^{+\infty} b_{i,j}^k \eta^i e^{-j\eta},\ \theta(\eta) = \sum_{k=0}^{+\infty}\sum_{i=0}^{+\infty}\sum_{j=0}^{+\infty} c_{i,j}^k \eta^i e^{-j\eta}, \tag{15}$$

where $a_{i,j}^k$, $b_{i,j}^k$, $c_{i,j}^k$ are the constant coefficients to be determined by HAM-based Mathematica package BVPh 2.0. HAM relies heavily on the solution expression of Equation (15) to select auxiliary linear operators and initial guesses. It is important to note that the $f(\eta)$, $g(\eta)$, $\theta(\eta)$ given by BVPh 2.0 contain three unknown convergence control parameters, d_0^f, d_0^g, d_0^θ. The series solution relies on these to ensure convergence. The mean residual errors of the kth-order approximations are defined as follows:

$$\zeta_k^f\left(d_0^f, d_0^g, d_0^\theta\right) = \frac{1}{N+1}\sum_{i=0}^{N}\left[N_f\left(\sum_{m=0}^{k} f_m\right)\Bigg|_{\eta = i\beta\eta}\right]^2, \tag{16}$$

$$\zeta_k^f\left(d_0^f, d_0^g, d_0^\theta\right) = \frac{1}{N+1}\sum_{i=0}^{N}\left[N_g\left(\sum_{m=0}^{k} f_m, \sum_{m=0}^{k} g_m\right)\Bigg|_{\eta = i\beta\eta}\right]^2, \tag{17}$$

$$\zeta_k^f\left(d_0^f, d_0^g, d_0^\theta\right) = \frac{1}{N+1}\sum_{i=0}^{N}\left[N_\theta\left(\sum_{m=0}^{k} f_m, \sum_{m=0}^{k} g_m, \sum_{m=0}^{k} \theta_m\right)\Bigg|_{\eta = i\beta\eta}\right]^2, \quad (18)$$

for the original governing Equations (7)–(9). An approximation of the kth order has a total error defined as follows:

$$\zeta_k^{tol}\left(d_0^f, d_0^g, d_0^\theta\right) = \zeta_k^f\left(d_0^f, d_0^g, d_0^\theta\right) + \zeta_k^g\left(d_0^f, d_0^g, d_0^\theta\right) + \zeta_k^\theta\left(d_0^f, d_0^g, d_0^\theta\right), \quad (19)$$

As a result of the kth-order approximation, the optimal values for d_0^f, d_0^g, d_0^θ can be determined as the minimum of the total error of ζ_k^{tol}. Consult the online BVPh 2.0 for details on specific operations (http://numericaltank.sjtu.edu.cn/BVPh.htm (accessed on 18 May 2013)).

3. Results Analysis and Discussion

This analysis involves a discussion of the impact of the many physical parameters generated in the proposed model. When $\gamma = 0$, $\phi = 0$, and $\sigma = 0$, it can be found that $f(\eta) = g(\eta)$ represents the axisymmetric Homann stagnation-point flow. When $\gamma = 0$ (axisymmetric), $\phi = 0$ (pure fluid), and $\sigma = 0$ (non-porous medium), $f''(0)$ = 1.311608, compared with $f''(0)$ = 1.311938 in Waini et al. [38], the relative error is not more than 0.8194%. As shown in Table 5, the values of the skin friction coefficients of Cf_x, Cf_y, and the local Nusselt number Nu_x with γ, ϕ, and σ when Pr $= 6.2$ are calculated compared with the results of Waini et al. [38]. Consequently, Table 5 demonstrates that the results of the present mass-based study ($w_1 = w_2 = 0$, pure water) are consistent with previous similar work on volume fraction ($\phi = \phi_1 = \phi_2 = 0$, pure water). All calculation cases are compared when the first (Cu) and second (Al_2O_3) nanoparticles have the same shape factor, namely $n_1 = n_2$.

Table 5. Skin friction coefficients of Cf_x, Cf_y and local Nusselt number Nu_x under values of γ, ϕ, and σ when Pr = 6.2.

γ	ϕ	σ	Cf_x (Ref. [50])	HAM 20th	Relative Error(%)	Cf_y (Ref. [50])	HAM 20th	Relative Error(%)	Nu_x (Ref. [50])	HAM 20th	Relative Error(%)
0	0	0	1.311938	1.311608	0.0252	1.311938	1.311608	0.0252	1.806069	1.810147	0.2258
5			3.038940	3.036096	0.0935	−0.894909	−0.902242	0.8194	3.938146	3.998352	0.2257
−5			−0.894909	−0.902242	0.8194	3.038940	3.036096	0.0935	3.074275	3.084240	0.3241

An analysis of the shape factor of nanoparticles as it relates to velocity distribution is shown in Figure 2, where $w_1 = w_2 = 10\ gr$, $w_f = 100\ gr$ = 0, σ = 0, Pr = 6.2, and γ = 0. First, velocity increases as the shape factor increases, and then it decreases as the shape factor decreases. Furthermore, disk-shaped nanoparticles ($n_1 = n_2 = 8.3$) have similar velocity profiles to brick-shaped nanoparticles ($n_1 = n_2 = 3.7$). Whenever η is large, the dimensionless velocity profile reaches the same value, which is limited to 1. Nanoparticle shape has a greater effect on velocity fields than temperature distribution. Figure 3 shows the effect of the shape factor on the temperature distribution of nanoparticles where $w_1 = w_2 = 10\ gr$, $w_f = 100\ gr$ = 0, σ = 0, Pr= 6.2, and γ =0. Figure 3 shows the effect of shape factor on temperature distributions of nanoparticles. In general, as the shape factor increases, temperature profiles decrease first and then increase, especially for disk nanoparticles. The image indicates that the shape factors of nanoparticles are not significantly different between these dimensionless temperature profiles. As η increases, the dimensionless temperature profile reaches a value limited to 0. Compared to temperature distribution, the shape factor of nanoparticles has a greater effect on the velocity field. Based on Figures 2 and 3, increasing the levels of nanoparticle shape factors leads to increases in velocity and decreases in temperature. Consequently, the hydrodynamic boundary layer

and thermal boundary layer become thinner. In these cases, the Prandtl number is fixed at 6.2, which does not account for variations.

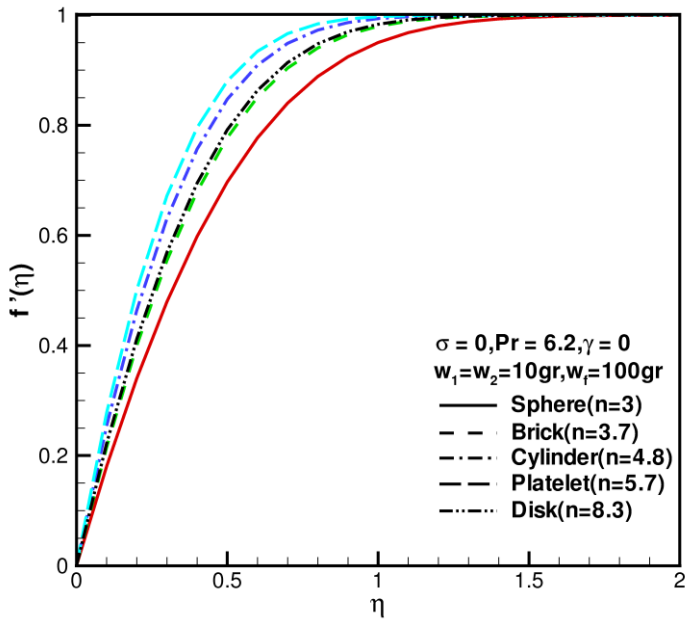

Figure 2. The dimensionless velocity component $f'(\eta)$ against the shape factor n when $w_1 = w_2 = 10$ gr, $w_f = 100$ gr, $\sigma = 0$, Pr = 6.2, and $\gamma = 0$.

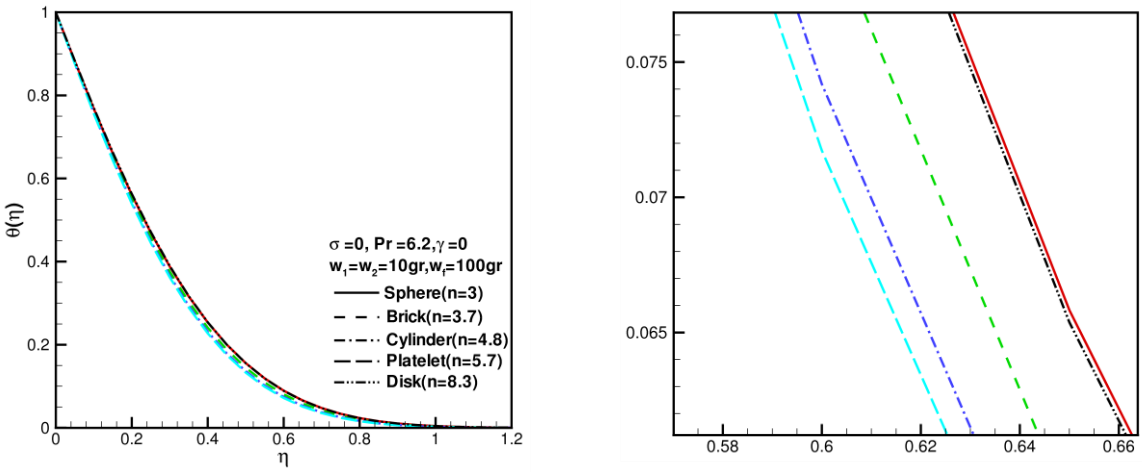

(**a**) (**b**)

Figure 3. The dimensionless temperature distributions $\theta(\eta)$ against shape factor n when $w_1 = w_2 = 10$ gr, $w_f = 100$ gr, $\sigma = 0$, Pr = 6.2, and $\gamma = 0$: (**a**) the full picture of $\theta(\eta)$; (**b**) the partial enlargement picture of $\theta(\eta)$.

When $w_1 = w_2 = 10\,gr$, $w_f = 100\,gr = 0$, $\sigma = 1$, Pr= 6.2, $\gamma = 0$, the effects of shape factor of nanoparticles on velocity, and temperature distributions $f\prime(\eta)$, $g\prime(\eta)$, $\theta(\eta)$ of hybrid nanofluid under different values of shear–strain rate ratios $\gamma = \pm 3$ are presented in Figures 4 and 5. The behaviors of flow fields by changing shear–strain rate ratios γ were studied. $f\prime(\eta), g\prime(\eta)$ increase with the increase in γ; $\theta(\eta)$ decreases with increase in γ. As shown in Figure 4, $f\prime(\eta)$ reverse flows occur near walls at $\gamma = -3$, or $g\prime(\eta)$ reverse flows occur near walls at $\gamma = 3$, the flow is inward near the stagnation zone. As the shape factor increases, the velocities increase first and then decrease. Moreover, the velocity profile of disk nanoparticles is close to that of brick nanoparticles. Figure 5 shows influence of shape factor of nanoparticles on temperature distributions. As shape factor n increases,

temperature profiles $\theta(\eta)$ decrease first and then increase; in particular, the temperature profile of disk nanoparticles is close to that of sphere nanoparticles because of the coefficient of permeability of porous medium $\sigma = 1$ increasing. This dimensionless temperature profile under the influence of the nanoparticle shape factor shows no significant difference.

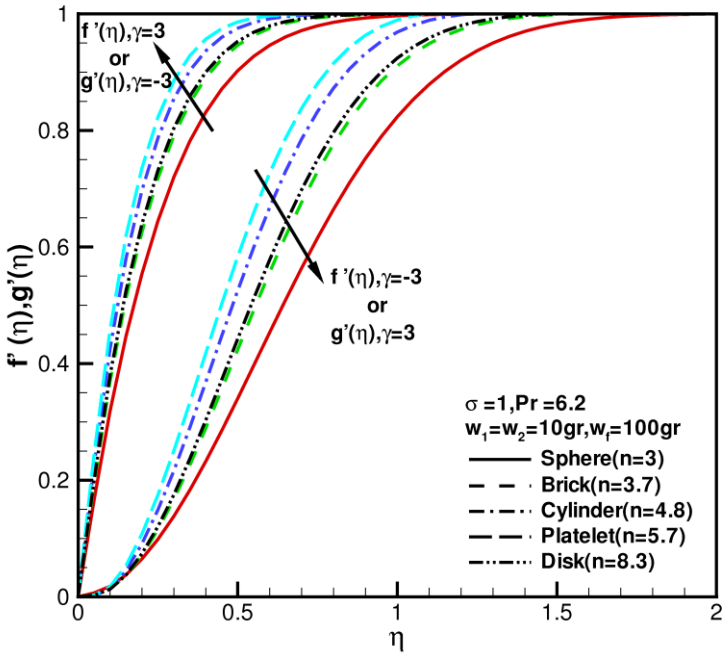

Figure 4. The dimensionless velocity components $f'(\eta)$, $g'(\eta)$ against shape factor n when $w_1 = w_2 = 10$ gr, $w_f = 100$ gr, $\sigma = 1$, Pr = 6.2, and $\gamma = -3, 3$.

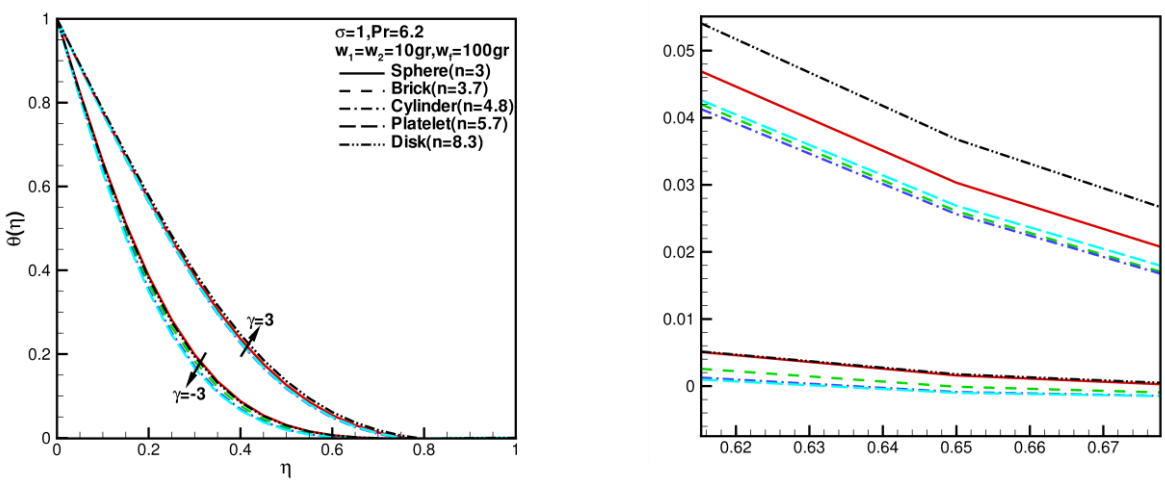

(**a**) (**b**)

Figure 5. The variations in dimensionless fluid temperature component $\theta(\eta)$ against the shape factor n when $w_1 = w_2 = 10$ gr, $w_f = 100$ gr, $\sigma = 1$, Pr = 6.2, and $\gamma = -3, 3$: (**a**) the full picture of $\theta(\eta)$; (**b**) the partial enlargement picture of $\theta(\eta)$; (**b**) the partial enlargement picture of $\theta(\eta)$.

In nanofluids or hybrid nanofluids, the shape of nanoparticles affects both thermal characteristics and flow characteristics. A plot showing the influence of the shape factor n of nanoparticles on the skin friction coefficients and local Nusselt number can be seen in Figure 6. The skin friction coefficients of Cf_x, Cf_y and the local Nusselt number Nu_x against γ in the range of $-6 \leq \gamma \leq 6$ for various shape factors $n_1 = n_2 = 3, 3.7, 4.8, 5.7$, and 8.3 when $w_1 = w_2 = 10$ gr, $w_f = 100$ gr, $\sigma = 0$, and Pr $= 6.2$ are shown in Figure 6. The values of Cf_x, Cf_y show a symmetric pattern where the line of symmetry lies at $\gamma = 0$ in the

axisymmetric case. When $\gamma = 0$, $\sigma = 0$, and $w_1 = w_2 = 0$, $Cf_x = f''(0) = 1.311608$, and $Cf_y = g''(0) = 1.311608$, also as shown in Table 5. As shown in Figure 6a, $Cf_x = Cf_y = 0$; that is, the wall shear stress value is 0 when $\gamma = \pm 2.50895$. When $\gamma < -2.50895$, Cf_x decreases with increasing w_1, w_2; when $\gamma > -2.50895$ increases, Cf_x increases with increasing w_1, w_2. When $\gamma > 2.50895$ increases, Cf_y decreases with increasing w_1, w_2; when $\gamma < 2.50895$, Cf_y increases with increasing w_1, w_2. Figure 6b shows the local Nusselt number Nu_x against γ in the range of $-6 \leq \gamma \leq 8$ for various shape factors $n_1 = n_2 = 3$, 3.7, 4.8, 5.7, and 8.3 when $w_1 = w_2 = 10$ gr, $w_f = 100$ gr, $\sigma = 0$, and Pr $= 6.2$. Nu_x increases as the value of the shape factor n increases. When $\gamma < 0$, the values of Nu_x increase sharply, with shape factor n increasing. When $\gamma > 0$, the values of Nu_x increase and slow down with an increase in shape factor n. In addition, for the axisymmetric case of $\gamma = 0$, when $w_1 = w_2 = 10$ gr, $w_f = 100$ gr, $\sigma = 0$, and Pr = 6.2, $Cf_x = Cf_y = 2.03443$, 1.69439, 1.42415, 1.29710, and 1.63776, changing with the shape factor $n_1 = n_2 = 3$, 3.7, 4.8, 5.7, and 8.3, as shown in Figure 7a. Among the five nanoparticle shapes, including spherical ($n_1 = n_2 = 3$), brick-shaped ($n_1 = n_2 = 3.7$), cylindrical ($n_1 = n_2 = 4.8$), platelet-shaped ($n_1 = n_2 = 5.7$), and disk-shaped ($n_1 = n_2 = 8.3$), spherical and platelet-shaped nanoparticles have the highest and lowest friction coefficients, respectively. Skin friction Cf_x, Cf_y decreases as the shape factor n increases. Among the five nanoparticle shapes, including spherical ($n_1 = n_2 = 3$), brick-shaped ($n_1 = n_2 = 3.7$), cylindrical ($n_1 = n_2 = 4.8$), platelet-shaped ($n_1 = n_2 = 5.7$), and disk-shaped ($n_1 = n_2 = 8.3$), the highest local Nusselt number is related to spherical nanoparticles, as shown in Figure 7b. Nu_x increases with an increase in shape factor n, showing a close correlation of the five nanoparticle shapes.

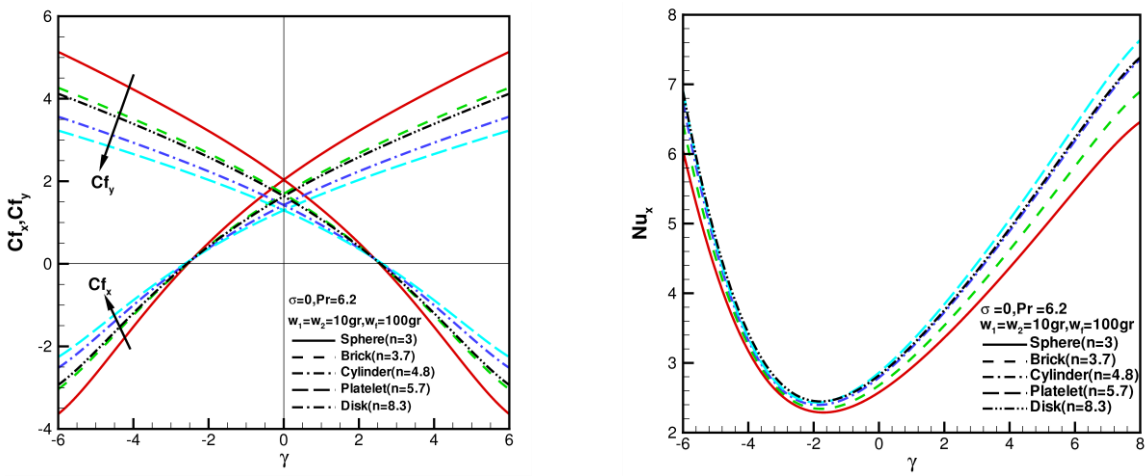

(**a**) (**b**)

Figure 6. Skin friction coefficients Cf_x, Cf_y and local Nusselt number Nu_x against γ, shape factor n when $w_1 = w_2 = 10$ gr, $w_f = 100$ gr, $\sigma = 0$, and Pr = 6.2: (**a**) the distributions of Cf_x, Cf_y; (**b**) the distributions of Nu_x.

When $w_1 = w_2 = 10$ gr, $w_f = 100$ gr, Pr $= 6.2$ $n_1 = n_2 = 3$ (spherical nanoparticles), the skin friction coefficients of Cf_x, Cf_y against γ in range of $-6 \leq \gamma \leq 6$ for various $\sigma = 0, 1, 2, 5$ are shown in Figure 8a. Additionally, for the axisymmetric case of $\gamma = 0$, when $w_1 = w_2 = 10$ gr, $w_f = 100$ gr, $Cf_x = Cf_y = 2.03443$, 2.27994, 2.50681, 3.10222 for various $\sigma = 0, 1, 2, 5$. Compared with $w_1 = w_2 = 10$ gr, $w_f = 100$ gr, $\sigma = 0$, it can be found that the wall shear stress values increase by 12.06%, 23.21%, and 52.48%, respectively. It is shown the percentage of skin friction coefficient enhanced by hybrid nanofluid relative to regular fluid. This shows that shear stress can be enhanced by increasing coefficient of permeability in porous media. As σ increases, the values of Cf_x and Cf_y increase. When $w_1 = w_2$ and γ are given certain values, the greater the values of σ, the stronger the values of Cf_x and Cf_y. When $w_1 = w_2 = 10$ gr, $w_f = 100$ gr, Pr $= 6.2 n_1 = n_2 = 3$ (spherical nanoparticles),

local Nusselt number Nu_x with γ in the range of $-6 \leq \gamma \leq 8$ for various σ = 0, 1, 2, 5 are shown in Figure 8b. As the coefficient of permeability in porous media increases, the values of Nu_x decrease when $\gamma < 0$. When $\gamma > 0$, the values of Nu_x are less affected by the values of σ.

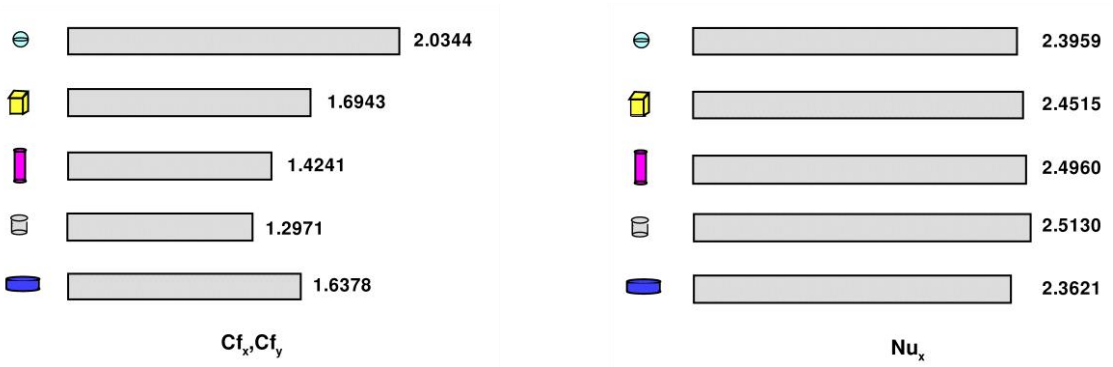

(**a**) (**b**)

Figure 7. Skin friction coefficients Cf_x, Cf_y and local Nusselt number Nu_x for various nanoparticle shapes when $w_1 = w_2$ = 10 gr, w_f = 100 gr, σ = 0, and Pr = 6.2: (**a**) the distributions of Cf_x, Cf_y; (**b**) the distributions of Nu_x.

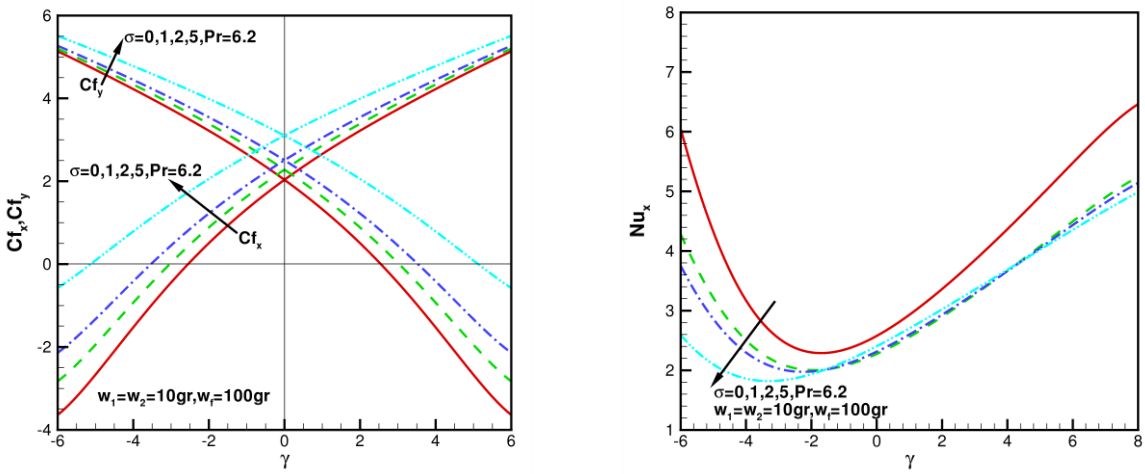

(**a**) (**b**)

Figure 8. Skin friction coefficients Cf_x, Cf_y and local Nusselt number Nu_x against γ when $w_1 = w_2$ = 10 gr, w_f = 100 gr, σ = 0, 1, 2, 5, and Pr = 6.2: (**a**) the distribution of Cf_x, Cf_y with $n1 = n2$ = 3 (sphere); (**b**) the distribution of Nu_x with $n_1 = n_2 = 3$ (sphere).

When w_1 = 10 gr, w_f = 100 gr, Pr $= 6.2$ $n_1 = n_2 = 3$ (spherical nanoparticles), skin friction coefficients of Cf_x, Cf_y with γ in the range of $-6 \leq \gamma \leq 6$ for various w_2 = 0, 10 gr, 30 gr, σ = 0, 1 are shown in Figure 9a. When w_1 = 10 gr, w_f = 100 gr, σ = 0, $Cf_x = Cf_y$ = 1.40293, 2.03443, 2.42377 for various w_2 = 0, 10 gr, 30 gr. Compared with w_1 = 10 gr, w_2 = 0, w_f = 100 gr, σ = 0, it can be found that the wall shear stress values increase by 45.01% and 72.76%, respectively. When w_1 = 10 gr, w_f = 100 gr, σ = 1, $Cf_x = Cf_y$ = 1.70784, 2.27994, 2.68638 for various $w2$ = 0, 10 gr, 30 gr. Compared with w_1 = 10 gr, w_2 = 0, w_f = 100 gr, σ = 0, it can be found that the wall shear stress values increase by 33.50% and 57.30%, respectively. This shows that shear stress can be augmented by increasing the mass of the second nanoparticle. When w_1 = 10 gr, w_f = 100 gr, Pr $= 6.2$ $n_1 = n_2 = 3$ (sphere nanoparticle), local Nusselt number Nu_x with γ in range of $-6 \leq \gamma \leq 8$ for various w_2 = 0, 10 gr, 30 gr, σ = 0, 1, 2 are shown in Figure 9b. As the mass of the second nanoparticle increases, Nu_x increases more evenly. With an increase in

the mass of the first and second nanoparticles of hybrid nanofluids, the relevant Nusselt number, and skin friction coefficient are enhanced. Since the mass of the nanoparticles increases, thermal conductivity is also augmented, affecting the rate of heat transfer.

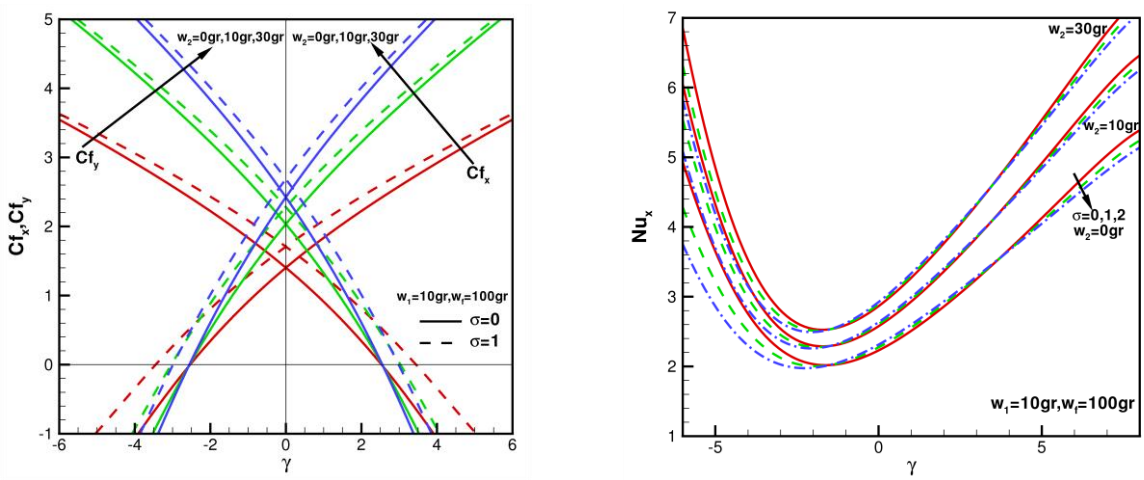

(**a**) (**b**)

Figure 9. Skin friction coefficients Cf_x, Cf_y and local Nusselt number Nu_x against γ when w_1 = 10 gr, w_f = 100 gr, w_2 = 0, 10 gr, 30 gr, σ = 0, 1, 2, 5, and Pr = 6.2: (**a**) the distribution of Cf_x, Cf_y with $n_1 = n_2 = 3$ (sphere); (**b**) the distribution of Nu_x with $n_1 = n_2 = 3$ (sphere).

4. Conclusions

The impact of the shape factor on mass-based hybrid nanofluid models for Homann stagnation-point flow in porous media was studied herein. The HAM-based Mathematica package BVPh 2.0 is suitable for determining the solution of coupled nonlinear ODEs with boundary conditions. Free online instructions for BVPh 2.0 are available (http://numericaltank.sjtu.edu.cn/BVPh.htm (accessed on 18 May 2013)). The analysis involved a discussion of the impact of the many physical parameters generated in the proposed model. The results show that the skin friction coefficients of Cf_x, and Cf_y increase with the mass of the first and second nanoparticles of hybrid nanofluids w_1 and w_2 and with the coefficient of permeability in porous media. For the axisymmetric case of γ = 0, when $w_1 = w_2$ = 10 gr and w_f = 100 gr, $Cf_x = Cf_y$ = 2.03443, 2.27994, 2.50681, and 3.10222 for σ = 0, 1, 2, and 5. Compared with $w_1 = w_2$ = 10 gr, w_f = 100 gr, and σ = 0, it can be seen that the wall shear stress values increase by 12.06%, 23.21% and 52.48%, respectively. According to the calculation results, platelet-shaped nanoparticles in mass-based hybrid nanofluid models can achieve maximum heat transfer rates and minimum surface friction. As the mass of the first and second nanoparticles of hybrid nanofluid models increases, the local Nusselt number Nu_x increases. Nu_x decreases and obviously changes with an increase in the coefficient of permeability in the range of $\gamma < 0$; otherwise, Nu_x is less affected in the range of $\gamma > 0$.

Author Contributions: Conceptualization, S.L. and X.Y.; methodology, software, and formal analysis, X.Y.; validation, investigation, and data curation, S.L.; writing—original draft preparation, S.L. and X.Y.; writing—review and editing, S.L. and X.Y. All authors have read and agreed to the published version of the manuscript.

Funding: NSFC (National Natural Science Foundation of China, No. 52174011; No.12002390).

Data Availability Statement: The manuscript includes all relevant data.

Conflicts of Interest: The authors declare no conflict of interest.

Nomenclature

$\overline{u}$, $\overline{v}$, $\overline{w}$	The velocity components
$\overline{u}_e$, $\overline{v}_e$, $\overline{w}_e$	The external flow velocities
$\overline{a}$, $\overline{b}$	The strain shear rates
$\overline{T}_\infty$	The ambient temperature
$\overline{T}_0$	The characteristic temperature
$\overline{K}$	The permeability of porous media
$\overline{k}$	The conductivity in temperature
c_p	The coefficient of specific heat capacity
A	Coefficient for non-spherical nanoparticles in the effective viscosity relation for nanoparticles of different shapes
B	Coefficient for non-spherical nanoparticles in the effective viscosity relation for nanoparticles of different shapes
n	Shape factor
Cf_x, Cf_y	Coefficients of skin friction
Nu_x	Nusselt number
A_1, A_2	Coefficients from hybrid nanofluids
Pr	The Prandtl number
Re_x, Re_y	The local Reynolds numbers
w_1	Mass of first nanoparticles of hybrid nanofluids
w_2	Mass of second nanoparticles of hybrid nanofluids
w_f	Mass of base fluid
Greek symbols	
ρ	The fluid density
μ	The dynamic viscosity
ϕ, ϕ_1, ϕ_2	Volume fraction of hybrid nanofluids
ψ	Sphericity of nanoparticles
γ	Ratio of shear–strain rate
σ	Coefficient of permeability

References

1. Chamkha, A.J. Unsteady laminar hydromagnetic flow and heat transfer in porous channels with temperature-dependent properties. *Int. J. Numer. Methods Heat Fluid Flow* **2001**, *11*, 430–448. [CrossRef]
2. Umavathi, J.C.; Chamkha, A.J.; Mateen, A.; Al-Mudhaf, A. Unsteady oscillatory flow and heat transfer in a horizontal composite porous medium channel. *Nonlinear Anal. Model. Control* **2009**, *14*, 397–415. [CrossRef]
3. Momin, G.C. Experimental investigation of mixed convection with water-Al_2O_3 & hybrid nanofluid in inclined tube for laminar flow. *Int. J. Sci. Technol. Res.* **2013**, *2*, 195–202.
4. Kasaeian, A.; Daneshazarian, R.; Mahian, O.; Kolsic, L.; Chamkhae, A.J.; Wongwise, S.; Pop, I. Nanofluid flow and heat transfer in porous media: A review of the latest developments. *Int. J. Heat Mass Tran.* **2017**, *107*, 778–791. [CrossRef]
5. Ali, A.R.I.; Salam, B. A review on nanofluid: Preparation, stability, thermophysical properties, heat transfer characteristics and application. *SN Appl. Sci.* **2020**, *2*, 1636. [CrossRef]
6. Khashi'ie, N.S.; Waini, I.; Arifin, N.M.; Pop, I. Unsteady squeezing flow of Cu-Al_2O_3/water hybrid nanofluid in a horizontal channel with magnetic field. *Sci. Rep.* **2021**, *11*, 14128. [CrossRef] [PubMed]
7. Sangapatanam, S.; Subbarayudu, K.; Reddy, B.A. Hybrid nanofluids development and benefits: A comprehensive review. *J. Therm. Eng.* **2022**, *8*, 445–455.
8. Modi, K.V.; Patel, P.R.; Patel, S.K. Applicability of mono-nanofluid and hybrid-nanofluid as a technique to improve the performance of solar still: A critical review. *J. Clean. Prod.* **2023**, *387*, 135875. [CrossRef]
9. Murshed, S.; Leong, K.; Yang, C. Enhanced thermal conductivity of TiO_2/water based nanofluids. *Int. J. Therm. Sci.* **2005**, *44*, 367–373. [CrossRef]
10. Timofeeva, E.V.; Routbort, J.L.; Singh, D. Particle shape effects on thermophysical properties of alumina nanofluids. *J. Appl. Phys.* **2009**, *106*, 014304. [CrossRef]
11. Jeong, J.; Li, C.; Kwon, Y.; Lee, J.; Kim, S.H.; Yun, R. Particle shape effect on the viscosity and thermal conductivity of ZnO nanofluids. *Int. J. Refrig.* **2013**, *36*, 2233–2241. [CrossRef]
12. Elias, M.M.; Miqdad, M.; Mahbubul, I.M.; Saidur, R.; Kamalisarvestani, M.; Sohel, M.R.; Hepbasli, A.; Rahim, N.A.; Amalina, M.A. Effect of nanoparticle shape on the heat transfer and thermodynamic performance of a shell and tube heat exchanger. *Int. Commun. Heat Mass Tran.* **2013**, *44*, 93–99. [CrossRef]

13. Vanaki, S.M.; Mohammed, H.A.; Abdollahi, A.; Wahid, M.A. Effect of nanoparticle shapes on the heat transfer enhancement in a wavy channel with different phase shifts. *J. Mol. Liq.* **2014**, *196*, 32–42. [CrossRef]
14. Ghadikolaei, S.S.; Yassari, M.; Sadeghi, H.; Hosseinzadeh, K.; Ganji, D.D. Investigation on thermophysical properties of TiO_2-Cu/H_2O hybrid nanofluid transport dependent on shape factor in MHD stagnation-point flow. *Powder Technol.* **2017**, *322*, 428–438. [CrossRef]
15. Sheikholeslami, M.; Sajjadi, H.; Delouei, A.A.; Atashafrooz, M.; Li, Z. Magnetic force and radiation influences on nanofluid transportation through a permeable media considering Al_2O_3 nanoparticles. *J. Therm. Anal. Calorim.* **2018**, *136*, 2477–2485. [CrossRef]
16. Benkhedda, M.; Boufendi, T.; Tayebi, T.; Chamkha, A.J. Convective heat transfer performance of hybrid nanofluid in a horizontal pipe considering nanoparticles shapes effect. *J. Therm. Anal. Calorim.* **2020**, *140*, 411–425. [CrossRef]
17. Shah, Z.; Ikramullah; Kumam, P.; Selim, M.M.; Alshehri, A. Impact of nanoparticles shape and radiation on the behavior of nanofluid under the Lorentz forces. *Case Stud. Therm. Eng.* **2021**, *26*, 101161. [CrossRef]
18. Khashi'ie, N.S.; Arifin, N.M.; Sheremet, M.; Pop, I. Shape factor effect of radiative Cu-Al_2O_3/H_2O hybrid nanofluid flow towards an EMHD plate. *Case Stud. Therm. Eng.* **2021**, *26*, 101199. [CrossRef]
19. You, X.; Li, S. Fully developed opposing mixed convection flow in the inclined channel filled with a hybrid nanofluid. *Nanomaterials* **2021**, *11*, 1107. [CrossRef]
20. You, X.; Li, S. Effect of nanoparticle sphericity on mixed convective flow of nanofluids in an inclined channel. *Pet. Sci. Bull.* **2021**, *6*, 604–613.
21. You, X. Nanoparticle sphericity investigation of Cu-Al_2O_3-H_2O hybrid nanofluid flows between inclined channels filled with a porous medium. *Nanomaterials* **2022**, *12*, 2552. [CrossRef]
22. Wanatasanappan, V.V.; Kanti, P.K.; Sharma, P.; Husna, N.; Abdullah, M.Z. Viscosity and rheological behavior of Al_2O_3-Fe_2O_3/water-EG based hybrid nanofluid: A new correlation based on mixture ratio. *J. Mol. Liq.* **2023**, *375*, 121365. [CrossRef]
23. Dinarvand, S.; Rostami, M.N. An innovative mass-based model of aqueous zinc oxide–gold hybrid nanofluid for von Ka´rma´n's swirling flow. *J. Therm. Anal. Calorim.* **2019**, *138*, 845–855. [CrossRef]
24. Berrehal, H.; Dinarvand, S.; Khan, I. Mass-based hybrid nanofluid model for entropy generation analysis of flow upon a convectively-warmed moving wedge. *Chin. J. Phys.* **2022**, *77*, 2603–2616. [CrossRef]
25. Rahimi, A.; Surendar, A.; Kasaeipoor, A.; Hooshmand, P.; Malekshah, E.H. Lattice Boltzmann simulation of nanofluid flow and heat transfer in a hollow multi-pipe heat exchanger considering nanoparticles' shapes. *Powder Technol.* **2018**, *339*, 974–984. [CrossRef]
26. Rao, Y.; Shao, Z.; Rahimi, A.; Kasaeipoor, A.; Malekshah, E.H. Study on fluid flow and heat transfer in fluid channel filled with KKL model-based nanofluid during natural convection using FVM. *Int. J. Numer. Methods Heat Fluid Flow* **2019**, *29*, 2622–2641. [CrossRef]
27. Soumya, D.O.; Gireesha, B.J.; Venkatesh, P.; Alsulami, M.D. Effect of NP shapes on Fe_3O_4-Ag/kerosene and Fe_3O_4-Ag/water hybrid nanofluid flow in suction/injection process with nonlinear-thermal-radiation and slip condition; Hamilton and Crosser's model. *Wave Random Complex* **2022**. [CrossRef]
28. Subray, P.V.A.; Hanumagowda, B.N.; Varma, S.V.K.; Hatami, M. The impacts of shape factor and heat transfer on two-phase flow of nano and hybrid nanofuid in a saturated porous medium. *Sci. Rep.* **2022**, *12*, 21864. [CrossRef]
29. Esfe, M.H.; Alidoost, S.; Esfandeh, S.; Toghraie, D.; Hatami, H.; Kamyab, M.H.; Ardeshir, E.M. Theoretical-Experimental study of factors affecting the thermal conductivity of SWCNT-CuO (25:75)/water nanofluid and its challenging comparison with CuO nanofluids/water aiming to improve the base fluid thermal conductivity. *Arab. J. Chem.* **2023**, *16*, 104689. [CrossRef]
30. Mandal, G.; Pal, D. Dual solutions of radiative Ag-MoS_2/water hybrid nanofluid flow with variable viscosity and variable thermal conductivity along an exponentially shrinking permeable Riga surface: Stability and entropy generation analysis. *Int. J. Simul. Model.* **2023**. [CrossRef]
31. Farooq, U.; Waqas, H.; Aldhabani, M.S.; Fatima, N.; Alhushaybari, A.; Ali, M.R.; Sadat, R.; Muhammad, T. Modeling and computational framework of radiative hybrid nanofluid configured by a stretching surface subject to entropy generation: Using Keller box scheme. *Arab. J. Chem.* **2023**, *16*, 104628. [CrossRef]
32. Li, X.; Tian, C.; Li, H.; Liu, X.; Zhang, L.; Hong, S.; Ning, N.; Tian, M. Combined effect of volume fractions of nanofillers and filler-polymer interactions on 3D multiscale dispersion of nanofiller and Payne effect. *Compos. Part A* **2022**, *152*, 106722. [CrossRef]
33. Qi, W.; Liu, M.; Wu, J.; Xie, Q.; Chen, L.; Yang, X.; Shen, B.; Bian, X.; Song, W. Promoting the thermal transport via understanding the intrinsic relation between thermal conductivity and interfacial contact probability in the polymeric composites with hybrid fillers. *Compos. Part B* **2022**, *232*, 109613. [CrossRef]
34. Adun, H.; Mukhtar, M.; Adedeji, M.; Agwa, T.; Ibrahim, K.H.; Bamisile, O.; Dagbasi, M. Synthesis and application of ternary nanofluid for photovoltaic-thermal system: Comparative analysis of energy and exergy performance with single and hybrid nanofluids. *Energies* **2021**, *14*, 4434. [CrossRef]
35. Adun, H.; Kavaz, D.; Dagbasi, M.; Umar, H.; Wole-Osho, I.L. An experimental investigation of thermal conductivity and dynamic viscosity of Al_2O_3-ZnO-Fe_3O_4 ternary hybrid nanofluid and development of machine learning model. *Powder Technol* **2021**, *394*, 1121–1140. [CrossRef]

36. Adun, H.; Kavaz, D.; Wole-Osho, I.; Dagbasi, M. Synthesis of Fe_3O_4-Al_2O_3-ZnO/water ternary hybrid nanofluid: Investigating the effects of temperature, volume concentration and mixture ratio on Specific heat capacity, and development of Hybrid machine learning for prediction. *J. Energy Storage* **2021**, *41*, 102947. [CrossRef]
37. Ariel, P.D. On extra boundary condition in the stagnation point flow of a second grade fluid. *Internat. J. Engrg. Sci.* **2002**, *40*, 145–162. [CrossRef]
38. Weidman, P.D. Non-axisymmetric Homann's stagnation-point flows. *J. Fluid Mech.* **2012**, *702*, 460–469. [CrossRef]
39. Weidman, P.D. Impinging rotational stagnation-point flows. *Int. J. Nonlinear Mech.* **2017**, *88*, 97–101. [CrossRef]
40. Dinarvand, S.; Hosseini, R.; Pop, I. Homotopy analysis method for unsteady mixed convective stagnation-point flow of a nano fluid using Tiwari-Das nano fluid model. *Int. J. Numer. Methods Heat Fluid Flow* **2016**, *26*, 40–62. [CrossRef]
41. Othman, N.A.; Yacob, N.A.; Bachok, N.; Ishak, A.; Pop, I. Mixed convection boundary-layer stagnation point flow past a vertical stretching/shrinking surface in a nanofluid. *Appl. Therm. Eng.* **2017**, *11*, 1412–1417. [CrossRef]
42. Abbas, N.; Saleem, S.; Nadeem, S.; Alderremy, A.A.; Khan, A.U. On stagnation point flow of a micro polar nanofluid past a circular cylinder with velocity and thermal slip. *Res. Phys.* **2018**, *9*, 1224–1232. [CrossRef]
43. Turkyilmazoglu, M. Unsteady flow over a decelerating rotating sphere. *Phys. Fluids* **2018**, *30*, 033601. [CrossRef]
44. Sharma, P.R.; Sinha, S.; Yadav, R.S.; Filippov, A.N. MHD mixed convective stagnation point flow along a vertical stretching sheet with heat source/sink. *Int. J. Heat Mass Tran.* **2018**, *117*, 780–786. [CrossRef]
45. Sadiq, M.A.; Khan, A.U.; Saleem, S.; Nadeem, S. Numerical simulation of oscillatory oblique stagnation point flow of a magneto micropolar nanofluid. *RSC Adv.* **2019**, *9*, 4751–4764. [CrossRef]
46. Ahmed, J.; Shahzad, A.; Farooq, A.; Kamran, M.; Khan, S.U.D.; Khan, S.U.D. Radiative heat transfer in Homann stagnation-point flow of hybrid nanofluid. *Appl. Nanosci.* **2020**, *10*, 5305–5314. [CrossRef]
47. Khan, A.U.; Saleem, S.; Nadeem, S.; Alderremy, A.A. Analysis of unsteady non-axisymmetric Homann stagnation point flow of nanofluid and possible existence of multiple solutions. *Physica A* **2020**, *554*, 123920. [CrossRef]
48. Mahapatra, T.R.; Sidui, S. Non-axisymmetric Homann stagnation-point flow of a viscoelastic fluid towards a fixed plate. *Eur. J. Mech. B Fluids* **2020**, *79*, 38–43. [CrossRef]
49. Khan, M.; Sarfraz, M.; Ahmed, J.; Ahmad, L.; Fetecau, C. Non-axisymmetric Homann stagnation-point flow of Walter's B nanofluid over a cylindrical disk. *Appl. Math. Mech.* **2020**, *41*, 725–740. [CrossRef]
50. Waini, I.; Ishak, A.; Pop, I. Symmetrical solutions of hybrid nanofluid stagnation-point flow in a porous medium. *Int. Commun. Heat Mass Tran.* **2022**, *130*, 105804. [CrossRef]
51. Liao, S. *Advances in the Homotopy Analysis Method*, 1st ed.; World scientific press: Singapore, 2013; pp. 361–400.
52. Farooq, U.; Zhao, Y.; Hayat, T.; Alsaedi, A.; Liao, S. Application of the HAM-based Mathematica package BVPh 2.0 on MHD Falkner-Skan flow of nano-fluid. *Comput. Fluids* **2015**, *111*, 69–75. [CrossRef]
53. Dinarvand, S.; Rostami, M.N.; Pop, I. A novel hybridity model for TiO_2-CuO/water hybrid nanofuid flow over a static/moving wedge or corner. *Sci. Rep.* **2019**, *9*, 16290. [CrossRef] [PubMed]